Synthesis and in vitro preliminary evaluation of prostate-specific membrane antigen targeted upconversion nanoparticles as a first step towards radio/fluorescence-guided surgery of prostate cancer

Axel Cordonnier, Damien Boyer, Sophie Besse, Rodolphe Valleix, Rachid Mahiou, Mercedes Quintana, Arnaud Briat, Mhammed Benbakkar, Frédérique Penault-Llorca, Aurélie Maisonial-Besset, et al.

ARTICLE

Synthesis and *in vitro* preliminary evaluation of prostate-specific membrane antigen targeted upconversion nanoparticles as a first step towards radio/fluorescence-guided surgery of prostate cancer

Received 00th January 20xx,
Accepted 00th January 20xx

DOI: 10.1039/x0xx00000x

Axel Cordonnier[a,b], Damien Boyer[b], Sophie Besse[a], Rodolphe Valleix[b], Rachid Mahiou[b], Mercedes Quintana[a], Arnaud Briat[a], Mhammed Benbakkar[d], Frédérique Penault-Llorca[a,c], Aurélie Maisonial-Besset[a], Benoit Maunit[a], Sébastien Tarrit[a], Magali Vivier[a], Tiffany Witkowski[a], Leslie Mazuel[a], Françoise Degoul[a], Elisabeth Miot-Noirault[a], Jean-Michel Chezal[a,*]

Over the last decade, upconversion nanoparticles (UCNP) have been widely investigated in nanomedicine due to their high potential as imaging agents in the near-infrared (NIR) optical window of biological tissues. Here, we successfully develop active targeted UCNP as potential probes for dual NIR-NIR fluorescence and radioactive-guided surgery of prostate-specific membrane antigen (PSMA)(+) prostate cancers. We designed a one-pot thermolysis synthesis method to obtain oleic acid-coated spherical $NaYF_4$:Yb,Tm@$NaYF_4$ core/shell UCNP with narrow particle size distribution (30.0 ± 0.1 nm, as estimated by SAXS analysis) and efficient upconversion luminescence. Polyethylene glycol (PEG) ligands bearing different anchoring groups (phosphate, bis- and tetra-phosphonate-based) were synthesized and used to hydrophilize the UCNP. DLS studies led to the selection of a tetra-phosphonate $PEG_{(2000)}$ ligand affording water-dispersible UCNP with sustained colloidal stability in several aqueous media. PSMA-targeting ligands (i.e., glutamate-urea-lysine derivatives called KuEs) and fluorescent or radiolabelled prosthetic group were grafted onto the UCNP surface by strain-promoted azide-alkyne cycloaddition (SPAAC). These UCNP, coated with 10 or 100% surface density of KuE ligands, did not induce cytotoxicity over 24 h incubation in LNCaP-Luc or PC3-Luc prostate cancer cell lines or in human fibroblasts for any of the concentrations evaluated. Competitive binding assays and flow cytometry demonstrated the excellent affinity of UCNP@KuE for PSMA-positive LNCaP-Luc cells compared with non-targeted UCNP@CO_2H. Furthermore, the binding of UCNP@KuE to prostate tumour cells was positively correlated with the surface density of PSMA-targeting ligands and maintained after ^{125}I-radiolabelling. Finally, a preliminary biodistribution study in LNCaP-Luc-bearing mice demonstrated the radiochemical stability of non-targeted [^{125}I]UCNP paving the way for future *in vivo* assessments.

1. Introduction

Prostate cancer (PCa) is one of the most common cancers, representing the 5th cause of cancer deaths in men worldwide. From 2006 to 2016, a 40% increase in the incidence rate of PCa has been observed, related to a growing and aging population.[1] Radical prostatectomy remains the most common treatment option for localized PCa. However, and regardless of the surgical approach implemented (i.e., open, laparoscopic or robot-assisted radical prostatectomy), there is always a strong possibility of complications, such as sexual or urinary dysfunctions, and/or biochemical recurrence, the latter being associated with an elevated risk of PCa local recurrence and progression. Despite advances in the preoperative delineation of tumours using multiparametric magnetic resonance imaging (mMRI),[2] surgeons face the challenge of clearly defining the tumour's borders in real-time during surgery, while preserving the neurovascular tissues. This contributes to a significant percentage of positive surgical margins, from 1 to >50%, depending on the stage of the disease, the surgical technique and/or the surgeon's experience.[3,4] In such situations, intraoperative imaging approaches could help the surgeon to improve tumour boundary delineation and resection, thereby reducing positive surgical margins and biochemical recurrence, ultimately improving the outcome of PCa patients.

Over the last few decades, a variety of positron emission tomography (PET) and single photon emission computed tomography (SPECT) probes have been developed for PCa detection, targeting cell membrane synthesis (e.g., [^{11}C] or [^{18}F]F-choline), amino acid transport (e.g., [^{18}F]FACBC) or the

[a.] *Université Clermont Auvergne, Inserm, Imagerie Moléculaire et Stratégies Théranostiques, UMR 1240, F-63000 Clermont-Ferrand, France.*
[b.] *Université Clermont Auvergne, Clermont Auvergne INP, CNRS, ICCF, F-63000 Clermont-Ferrand, France.*
[c.] *Department of Pathology and Biopathology, Jean Perrin Comprehensive Cancer Centre, Clermont-Ferrand, France.*
[d.] *Université Clermont Auvergne, CNRS, Laboratoire Magmas et Volcans, UMR 6524, F-63000 Clermont-Ferrand, France.*
† Electronic Supplementary Information (ESI) available: [details of any supplementary information available should be included here]. See DOI: 10.1039/x0xx00000x

prostate-specific membrane antigen (PSMA) (e.g., [^{68}Ga]Ga-, [^{99m}Tc]Tc- or [^{18}F]F-PSMA inhibitor).[5,6] These new radiotracers have shown great promise for improved diagnosis, high-risk patients staging, biochemical recurrence follow-up and preoperative tumour mapping in combination with CT or MRI.[7,8] However, these imaging agents seem to be limited for the intraoperative localization of tumour sites because of the low spatial resolution of the hand-held PET or gamma probes used for radio-guided surgery. Conversely, Near-Infrared (NIR) fluorophores specifically designed to target PCa cells, offer the advantage of real-time visual imaging for intraoperative purposes, but their lower tissue penetration depth makes them unsuitable for whole-body imaging. To overcome these limitations, radionuclide and NIR fluorescence imaging can be combined to benefit from the advantages of both technologies. Different approaches have been explored, notably in hybrid tracers for which the fluorescence emission was generated by means of external excitation or γ-radiation and/or Cherenkov luminescence emitted by the radionuclide itself.[9,10,11,12,13,14,15] Among the broad range of conventional NIR fluorophores that can be used for such applications, organic dyes have been the most extensively studied in clinical trials.[16] However, NIR organic dyes are relatively large molecules and their conjugation with small radiolabelled tumour-targeting ligands may have a negative effect on the pharmacokinetic profile; in-depth structure-relationship studies are therefore necessary. NIR organic probes may also be subject to biological degradation, fluorescent instability and/or radioactive sensitivity, leading to extensive research to circumvent these limitations.[17,18] To our knowledge, hybrid probes for radio/NIR fluorescence-guided surgery of PCA have only been studied in a few preclinical proof-of-concept studies, with promising results.[19,20,21]

Compared with conventional NIR fluorophores, lanthanide-doped upconversion nanoparticles (UCNP) present many advantages, such as sharp emission bandwidths, large anti-Stokes shift, enhanced photostability, long luminescence lifetime, and low toxicity.[22,23] UCNP are also easily tunable in term of wavelength emission, shape and size. Depending on the dopants and host lattice used, nanoparticles can convert two or more NIR low energy photons (typically 980 or 808 nm) into shorter NIR to visible wavelength emissions. Properly functionalized, the particle surface could also be a versatile platform for introducing cell-specific targeting ligands, drugs and/or radionuclides for bioimaging or theranostic purposes. In cancerology, these unique properties of UCNP were exploited for a broad range of applications, including *in vitro*/*in vivo* cell tracking, *in vivo* fluorescence imaging of tumour alone or combined with magnetic resonance imaging, computed tomography, nuclear medicine imaging, chemotherapy, photo-thermal or dynamic therapy, drug delivery, to name a few.[24-27]

On the basis of our previous study on *in vivo* fluorescence imaging of dendronized UCNP,[28] this paper reports our preliminary results on the synthesis of NIR fluorescent $NaYF_4$:Yb,Tm@$NaYF_4$ core/shell UCNP coated with oleic acid (OA), using an original, one-pot procedure, and their hydrophilization with a series of PEGylated phosphate, bis- and tetra-phosphonate ligands to convert these hydrophobic UCNP into biocompatible nanomaterial. We describe the bioorthogonal conjugation of optimized UCNP@PEG with different surface densities of PSMA-targeting ligands and *in vitro* assessment of the active targeting in PSMA positive prostate tumour cells. The biodistribution profile of non-targeted ^{125}I-radiolabelled UCNP in prostate cancer mouse model is also evaluated to assess *in vivo* labelling stability.

2. Materials and Methods

2.1. Materials and Reagents

All chemical reagents for the synthesis of UCNP were purchased from Sigma-Aldrich. All rare earth chlorides utilized were 99.9% purity or higher. Oleic acid (90%) was stored at 4 °C before used. 2-(Phosphonomethyl)pentanedioic acid (PMPA) and DBCO-PEG_4-5/6-FAM (λ_{ex} 492 nm, λ_{em} 517 nm) were purchased from Interchim and Jena Bioscience, respectively. All nanoparticles filtrations were done on Chromafil Xtra PTFE-20/13 (Macherey-Nagel). Size exclusion purification was performed using prepacked PD-10 column (Sephadex G-25M, GE Healthcare Life Sciences). The UCNP purification by ultracentrifugation after ligand exchange or functionalization procedures was performed with Amicon ultra-15 tubes (30 kDa, Merck Millipore).

2.2. UCNP characterization

X-ray diffraction (XRD) patterns were recorded on UCNP powder samples at room temperature with an X'Pert pro diffractometer (Panalytical) using Cu Kα radiation in a 2θ range from 10 to 90 degrees. To perform transmission electron microscopy (TEM), 10 µL sample solution was deposited on Carbon-Formvar copper grids and dried at room temperature. Samples were observed using a Hitachi transmission electron microscope (H-7650) at 80 kV acceleration voltage. Micrographs were made using a Hamamatsu camera placed in a side position. Small angle X-ray scattering (SAXS) measurements were performed on a goniometer-based X-ray scattering platform (Empyrean Nano edition, Malvern Panalytical) instrument using Cu Kα radiation in the transmission mode in a 2θ range from -0.11 to 8 degrees. Liquid based samples were prepared by drawing colloidal solutions into a 1 mm outer diameter (0.01 mm wall thickness) quartz capillaries and then were flamed to avoid moisture presence. A pure solvent without UCNP (i.e., cyclohexane) in the same capillary was used for background subtraction. The concentration for all samples was approximately 1 mg/mL. All the data analyses were performed using EasySAXS (Malvern Panalytical) software. Dynamic light scattering (DLS) were carried out on a Zetasizer Nano ZS (Malvern Instruments). For DLS analysis, solutions of nanoparticles (1 mg/mL in deionized water or cyclohexane, unless otherwise specified) were filtered through a 0.2 µm PTFE filter (washed beforehand with 1 mL of the appropriate solvent) before analysis at 20 °C with a measured angle of 173° and a 633 nm laser. Photoluminescence upconversion spectra were performed on solutions of UCNP in cyclohexane or deionized water (1 mg/mL) and obtained using a CNI FC-980-5.2W diode

laser and analyzed with a TRIAX 550 Jobin-Yvon/Horiba monochromator. ICP-MS analyses were performed on NexION 350D (PerkinElmer) instrument while ICP-OES analyses were done on Jobin-Yvon ULTIMA C (HORIBA). Prior to both ICP-MS and ICP-OES analysis, UCNP were lyophilized and mineralized in concentrated nitric acid (65% in water, Sigma Aldrich) at 100 °C overnight then diluted to 10 mL with deionized water. FTIR spectra were collected at room temperature with a spectrometer Nicolet 5700 FTIR. Thermogravimetric analyses (TGA) were performed on lyophilized nanoparticles using a SETSYS Evolution TG-ATD DSC instrument. Nanoparticles were heated to 100 °C in air (10 °C/min), held isothermally for 30 min and were then heated to 800 °C (10 °C/min). Preliminary TGA was performed on pure ligands to take into account incomplete decomposition of the organic counterpart of UCNP using the equation: $w_{l,c} = w_l/(1-w_r)$ where w_l is the mass fraction of ligands covering UCNP and w_r is the residual weight fraction of pure ligands.

2.3. One-pot two-step synthesis of 980-excited core/shell UCNP@OA

The first step was to synthesize the core nanoparticles with a $NaY_{0.78}Yb_{0.20}Tm_{0.02}F_4$ composition. To a 100 mL three-neck round-bottom flask containing a mixture of OA (6 mL) and octadecene (15 mL) were successively added under stirring YCl_3 (152.3 mg, 780 μmol), $YbCl_3$ (55.9 mg, 200 μmol) and $TmCl_3$ (5.5 mg, 20 μmol). The solution was heated under stirring at 150 °C for 30 min to form a homogenous solution. Freshly prepared solutions of NaOH (100 mg, 2.5 mmol) in methanol (10 mL) and NH_4F (148 mg, 4.00 mmol) in methanol (10 mL) were sonicated for 5 min, pooled and added to the reaction mixture cooled to 60 °C. The resulting solution was heated at 110 °C for 20 min then under vacuum for 10 min to remove volatile solvent. The flask was then filled with argon and heated at 302 °C for 1 h (heating rate 10 °C/min). In order to cover the cores with an undoped $NaYF_4$ shell, after cooling down to 40 °C, YCl_3 (111.9 mg, 573 μmol) was added and the reaction mixture was heated at 150 °C for 30 min. Freshly prepared solutions of NaOH (57.3 mg, 1.44 mmol) in methanol (5 mL) and NH_4F (84.8 mg, 2.29 mmol) in methanol (5 mL) were sonicated for 5 min, pooled and added to the reaction mixture cooled to 60 °C. The resulting solution was heated under stirring at 110 °C for 20 min then under vacuum for 10 min to remove volatile solvent. The flask was then filled with argon and heated under stirring at 302 °C for 1.5 h (heating rate 10 °C/min). After cooling down to room temperature, the reaction mixture was transferred into a PTFE centrifuge tube and the UCNP were purified by three sedimentation-redispersion cycles involving precipitation by the addition of ethanol (25 mL), centrifugation (6666 g, 10 min, 22 °C, Sigma 3-18K centrifuge), discarding of the supernatant and redispersion in cyclohexane (20 mL). Finally, the resulting solution was centrifuged (999 g, 5 min, 22 °C, Sigma 3-18K centrifuge) and the supernatant containing core/shell UCNP@OA (180-200 mg per batch) was stored for further use at room temperature at a final concentration of ca. 10 mg/mL in cyclohexane.

2.4. Ligand exchange on the surface of UCNP

A solution of UCNP@OA in cyclohexane (1 mg/mL, 20 mL) was sonicated for 30 min and volatiles were evaporated under reduced pressure. The residue was taken up in anhydrous tetrahydrofuran (5 mL) and transferred into a sealed vial. PEG ligand (200 mg) was then added under argon and the reaction solution was magnetically stirred at 40 °C for 16 h. After cooling down to room temperature, the solution was transferred into a PTFE centrifugal tube, the vial was rinsed with tetrahydrofuran (5 mL) and UCNP@PEG were precipitated by adding cyclohexane (40 mL). The mixture was vortexed for 1 min and then centrifuged (7499 g, 40 min, 22 °C, Sigma 3-18K centrifuge) to form a pellet. The supernatant was discarded, and the same cycle of precipitation/centrifugation was repeated once. After removal of the supernatant, the pellet was dried at room temperature using a gentle stream of argon. The resulting hydrophilic UCNP@PEG were dissolved in deionised water (15 mL) and concentrated to 0.3-0.5 mL by ultrafiltering through a spin filter with a 30 kDa molecular weight cut-off (4000 g, 15 min, 20 °C, Eppendorf 5804 R). This water dilution/concentration step was repeated twice. The UCNP@PEG were finally stored for further use at 4 °C in deionised water at a final concentration of ca. 10 mg/mL.

2.5. Colloidal stability study

Aqueous solutions of UCNP@PEG (ca. 10 mg/mL) were sonicated for 30 min. An aliquot (100 μL) of each solution was diluted with 1.4 mL of the appropriate media (i.e., deionized water, saline, PBS, MEM or RPMI) to reach a final concentration of ca. 0.67 mg/mL. The resulting solution was filtered through a 0.2 μm PTFE filter (washed beforehand with 1 mL of the appropriate media) and analysed by DLS at 20 °C (for deionized water, saline and PBS) or 37 °C (for MEM and RPMI cell culture media).

2.6. Surface functionalization of UCNP by bioorthogonal coupling reactions

UCNP functionalization was performed using the following procedure: to an aqueous solution of UCNP@N_3 (10 mg/mL) was added a solution of ADIBO-KuE(1-3) in deionized water (10 nmol/μL) or ADIBO-CO_2H (compound S33, ESI) in DMSO (10 nmol/μL). UCNP@$N_{3(10\%)}$ and UCNP@$N_{3(100\%)}$ were reacted with 5 eq. and 2 eq. of ADIBO derivatives, respectively. Each solution was incubated overnight at 37 °C in an oven. The excess of ADIBO derivatives was removed by size exclusion chromatography (PD-10 column, water elution) followed by two cycles of ultracentrifugation over 30 kDa MW cut-off membrane (Amicon ultra-15). Filtrate was finally diluted in saline to an approximate concentration of 10 mg/mL further corrected by UCNP drying and weighting. Whenever required, DBCO-PEG_4-5/6-FAM fluorescent dye in DMSO (4 nmol/μL) was mixed-up with ADIBO-KuE/CO_2H solutions at a molar ratio of 0.5/99.5, before adding to UCNP@N_3 solution. For UCNP radiolabelling, a solution of [^{125}I]IBA-ADIBO in DMSO was added to the UCNP@N_3 solution (~ 740 kBq/mg of UCNP) and heated at 37

°C for 30 min prior to the addition of ADIBO-KuE/CO_2H solutions.

2.7. *In vitro* studies

2.7.1. Cell culture conditions

Human prostate cancer cell lines, LNCaP-Luc (PSMA positive) and PC3-Luc (PSMA negative) were obtained from Perkin Elmer (Villebon sur Yvette, France) while human fibroblast cells were purchased from Promocell (Heidelberg, Germany). LNCaP-Luc were cultured in RPMI 1640 medium (Invitrogen, Villebon sur Yvette, France) supplemented with 10% fetal bovine serum (FBS) (Eurobio, Courtaboeuf, France) and 4 µg/mL gentamycin (Invitrogen). PC3-Luc were cultured in MEM Glutamax medium (Invitrogen) supplemented with 10% FBS and 2 µg/mL puromycin (Invivogen, Toulouse, France). Fibroblasts were cultured in MEM Glutamax medium containing 10% FBS, nonessential amino acids 1% (Invitrogen), 1 mM sodium pyruvate (Invitrogen), vitamins 1% (Invitrogen) and 4 µg/mL gentamycin. Cells were incubated at 37 °C in a humidified incubator in the presence of 5% CO_2 and were mycoplasma free.

2.7.2. *In vitro* cytotoxicity assessment of UCNP

UCNP cytotoxicity was examined by resazurin assay on LNCaP-Luc and PC3-Luc prostate cancer cells and human fibroblasts. Cells were seeded in 24-well plates at a density of $3x10^4$ cells per well for 48 h. Cell culture medium was replaced by fresh complete medium containing increasing concentrations of functionalized UCNP (0.12 µg-1.2 mg/mL and 0.17 µg-1.7 mg/mL, for 10 and 100% coverage, respectively). After 24 h of incubation at 37 °C, the medium was removed and replaced by resazurin solution in MEM medium without phenol red (800 µL, 25 µg/mL) for 1 h. The fluorescence (530 nm (λ_{ex}) / 590 nm (λ_{em})) was measured using a microplate reader (Fluoroskan, Labsystems).

2.7.3. *In vitro* competition binding experiments

LNCaP-Luc cells were seeded in 24-well plate at a density of $15x10^4$ cells per well for 48 h. After removal of growth media, the cells were washed with binding buffer (300 µL, RPMI 1640 Glutamax, 0.5% BSA). 2-[3-[1-carboxy-5-(4-[^{125}I]iodobenzoylamino)pentyl]ureido]pentanedioic acid ([^{125}I]IBA-KuE)[29] (detailed protocol are provided in the ESI) was added to a final concentration of 0.45 nM in the presence of increasing concentrations of ADIBO-KuE conjugates (1 nM-10 µM), PMPA (1 nM-10 µM) or UCNP@KuE (10 pM-100 nM) in binding buffer (final volume of 300 µL). After 1 h of incubation at 37 °C, binding buffer was removed and cells were washed with binding buffer (300 µL). Cells were lysed in RIPA buffer (50 mM Tris-HCl pH 7.5, 150 mM NaCl, 1% NP-40, 0.5% sodium deoxycholate, 0.1% SDS), washed with PBS (1 mL) and counted using a 1480 WIZARD Automatic Gamma Counter (Perkin Elmer). Half-maximum inhibition constants (IC_{50}) were determined using GraphPad (GraphPad 9.0, San Diego, USA) and are given as mean ± SD.

2.7.4. Flow cytometry assay

After trypsinization $5x10^5$ LNCaP-Luc cells were incubated with the different FAM conjugated UCNP (UCNP@KuE(1-3), UCNP@CO_2H) at a final concentration of 1.2 mg/mL in growth medium for 30 min at 4 °C. The cells were then washed three times with PBS-2% FBS, and collected by centrifugation (500 g, 5 min, 4 °C). Finally, cells were suspended in 200 µL of PBS/2% FBS and samples were analysed using a flow cytometer (BD Accuri C6 Plus, BD Biosciences). Statistical analyses were performed with the GraphPad Prism software. An ANOVA analysis was used with a confidence interval of 95%, p value < 0.05 was considered to be statistically significant.

2.7.5. Cellular uptake

For cellular uptake, LNCaP-Luc cells were seeded in 24-well plate at a density of $15x10^4$ cells per well for 48 h. Cells were incubated with 18.5 kBq of [^{125}I]UCNP@KuE3 or [^{125}I]UCNP@CO_2H in growth medium for 60 min at 37 °C and 5% CO_2. After incubation, the medium was quickly removed, the cells were washed with cold PBS, and trypsinized. After centrifugation (450 g, 5 min, 4 °C), pellets were counted for radioactivity using a 1480 WIZARD Automatic Gamma Counter (Perkin Elmer). Results are given as mean of % incubated dose ± SD.

2.8. *In vivo* biodistribution

Animal experiments were conducted in compliance with the 2010/63/UE European Directive and authorized by the French Ministry of Research after approval by the local ethical committees (authorization number #18209). Four weeks old NMRI nude male mice were purchased from Janvier Labs (Le Genest-Saint-Isle, France) and housed in standard conditions (n = 5 per cage on ventilated racks, at 24 °C, 60% humidity, 12 h light/12 h dark cycle) with *ad libitum* access to food and water. For establishment of xenografts, mice were injected subcutaneously with $10x10^6$of cells suspended in 200 µL of PBS/Matrigel (Corning® Matrigel® Basement Membrane Matrix High Concentration, reference 354248, Dutscher, Brumath, France) in a 1:1 ratio in the right flank of the animals.

In vivo biodistribution studies of radiolabelled non functionalized UCNP (i.e., [^{125}I]UCNP@$CO_2H_{(10\%)}$) were undertaken at day 71 after tumour inoculation, when animals exhibited tumour volume of approximately 500 mm^3. The [^{125}I]UCNP@$CO_2H_{(10\%)}$ in saline were administrated intravenously (i.v.) in the tail vein (0.39 ± 0.06 MBq/animal) and animals (n = 3 per time points) were sacrificed by CO_2 asphyxiation at several time points (5 min, 1 h, 3 h, 24 h and 48 h). Tumours and major organs were excised, harvested, weighted and their radioactivity counted using a 1480 WIZARD Automatic Gamma Counter (Perkin Elmer). Results were expressed as %injected dose per gram of organs (%ID/g) except for thyroid (%ID).

3. Results and discussion

3.1. Synthesis and characterization of core/shell $NaYF_4$:Yb,Tm@$NaYF_4$ UCNP@OA

As mentioned above, rare-earth UCNP present a broad spectrum of excitation/emission wavelengths from ultra-violet to NIR, depending on the host lattice, lanthanide sensitizer and activator ions, size distribution, shape, surface ligands, etc.[22] NIR-to-NIR UCNP have been preferred for *in vivo* fluorescence imaging applications to increase the penetration depth in tissues and organs, and to reduce autofluorescence background in complex physiological media, while minimizing photo-damage to cells.[23,30] Bearing in mind these criteria, we developed narrow size distribution core/shell $NaYF_4$:Yb,Tm@$NaYF_4$ UCNP coated with OA, and exhibiting a strong 800 nm emission upon continuous 980 nm laser excitation.

To shorten the reaction time, UCNP@OA synthesis was carried out using an original, batch to batch reproducible, one-pot procedure, and compared in terms of physicochemical and optical properties to our previously described standard two steps synthesis[28] (see detailed protocol and Fig. S3, ESI). Calculation of the reactant quantities for shell synthesis were based on our previous results, assuming that all reactants were consumed by the end of the first reaction step to produce monodisperse and spherical core nanoparticles.

As shown from the XRD pattern in Fig. 1a, the core/shell UCNP@OA crystallized in the hexagonal phase (ICDD 16-0334). TEM analysis (Fig. 1b) highlighted the homogeneous spherical shape and narrow size distribution of the nanoparticles (29 ± 2 nm). Unlike TEM analysis, the small angle X-ray scattering technique allows particle size measurement for a larger number of nanoparticles (up to 7 orders of magnitude) and avoids issues stemming from the drying procedure (aggregation etc.). Fig. 1c presents the scattering curve obtained from a suspension (1 mg/mL) of core/shell UCNP@OA in cyclohexane. Several narrow, clear-cut oscillations are visible on the SAXS data, indicating that the sample is very homogeneous in terms of shape and size. After fitting the data obtained to a noninteracting spherical particle model (red curve Fig. 1c), the average diameter was estimated at 30.0 ± 1.0 nm, with a low size polydispersity (RSD 7%). This value is consistent with both the TEM diameter and the pair distance distribution function (ρ(r)), which correspond to the real-space equivalent to the scattering curves (I(q)). As expected, the hydrodynamic diameter of UCNP@OA in cyclohexane determined by DLS is slightly higher than TEM and SAXS diameters (44.2 nm, PDI = 0.192, Fig. 1d). Finally, the upconverting luminescence (UCL) spectra recorded from 650 nm to 900 nm (Fig. 1e) and elemental compositions determined by ICP-MS analyses (Fig. 1f) were found to be similar, regardless of the synthesis method employed. A full UCL spectrum of UCNP@OA obtained from the one-pot procedure and recorded in the 420-900 nm range is presented in Figure S7a (ESI) with all the transitions of Tm^{3+} ions. Taken together, these results confirm the relevance of our one-pot protocol, with its excellent batch-to-batch reproducibility, shorter procedure time and preservation of UCNP physicochemical properties.

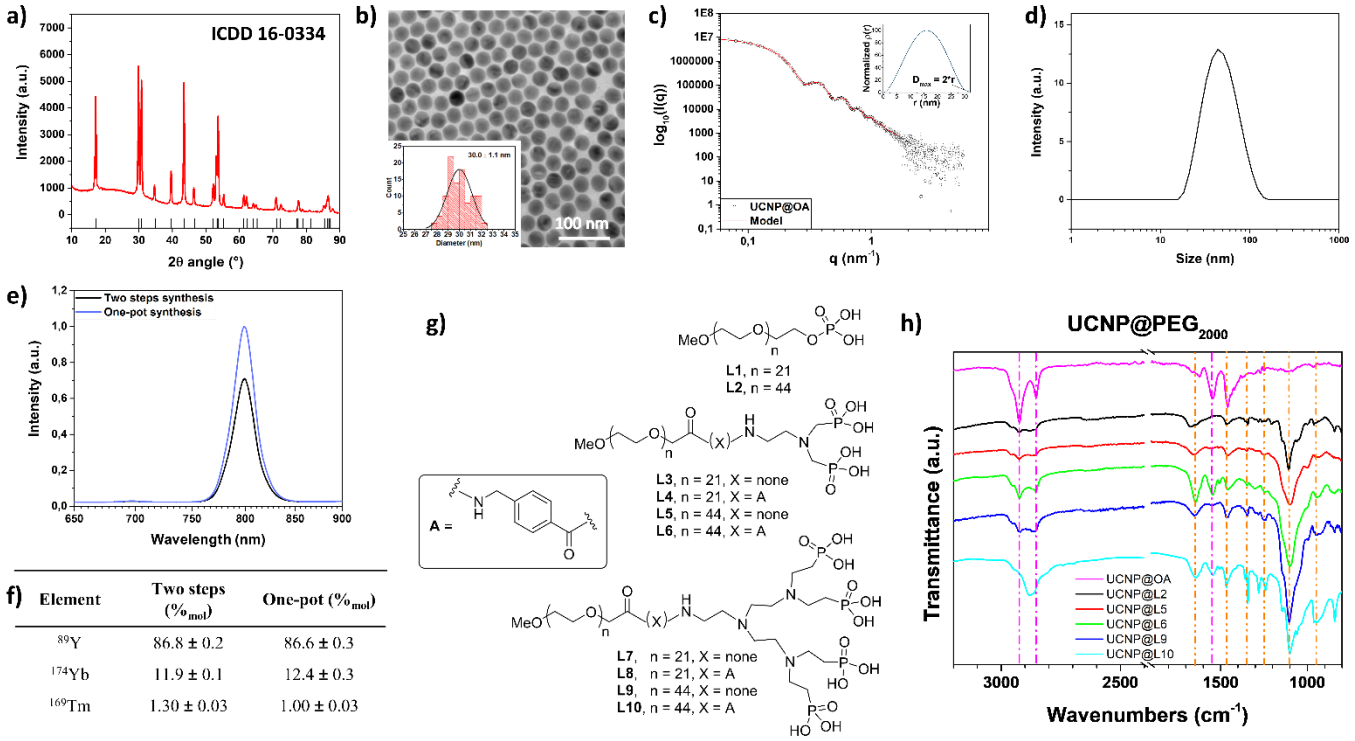

Fig. 1 Characterization of core/shell UCNP@OA obtained from one-pot synthesis: (**a**) XRD pattern, (**b**) TEM image and histogram of the size distribution, (**c**) SAXS data (in cyclohexane), (**d**) DLS distribution in cyclohexane, (**e**) normalized upconversion luminescence spectra recorded under 980 nm excitation at a concentration of 1 mg/mL in cyclohexane (luminescence spectra under the same conditions of UCNP@OA obtained from the two steps process was given for comparison); (**f**) ICP-MS elemental quantifications (elemental analysis of UCNP@OA obtained from the two steps procedure was also given); (**g**) PEG ligands L1-10 used for UCNP hydrophilization; (**h**) ATR-FTIR spectra of UCNP before (UCNP@OA) and after ligand exchange with $PEG_{(2000)}$ ligands (UCNP@L2, @L5, @L6, @L9 and @L10). Magenta dashed lines highlight OA =C-H and C=O bands, while orange dashed lines were assigned to PEG backbone bands.

3.2. Synthesis of PEG ligands, ligand exchange and colloidal stability study

One challenging issue for *in vivo* applications is the conversion of hydrophobic UCNP coated with OA into biocompatible materials. The surface coating must ensure long-term colloidal stability in physiological media, limited interaction with serum proteins, and easy chemical functionalization for grafting both tumour-targeting ligands and radioactive probes. The choice of both polymer and anchoring group is therefore of the utmost importance for the formation of stable, hydrophilic, polymer-coated UCNP. Among the broad range of strategies that can be employed (ligand removal or oxidation, silanization, layer-by-layer assembly, amphiphilic polymer coating, etc.), exchange of the OA surface coating using an excess of mono- or polydentate hydrophilic ligands under optimal conditions (solvent, temperature, time) is by far one of the most widely used.[25,26] Exploiting the hydrophilicity, non-immunogenicity and low toxicity of PEG polymers[31] as well as the ability of phosphate or phosphonate groups to bind the positively charged surface of UCNP with higher electrophilic interactions than carboxylate function, a wide range of water-dispersible PEG-(mono or poly)phosphate or phosphonate lanthanide-based UCNP have recently been reported.[32,33,34,35] To implement this strategy with our $NaYF_4$ host lattice, we synthesized ten polymers with different anchoring groups (i.e., phosphate, bis- and tetra-phosphonate) and PEG chain lengths (i.e., 1000 or 2000 molecular weight) (Fig. 1g).

The aim of this initial study was to assess the colloidal stability of PEGylated UCNP after ligand exchange, in several aqueous media, bearing in mind that a functional group can be introduced instead of the inert methoxy chain-end group for further surface functionalization. To obtain the m-$PEG_{(1000\ or\ 2000)}$-phosphoric acid derivatives, L1 and L2, we implemented a three-step synthesis procedure, involving phosphoramidite/tetrazole phosphitylation of commercially available m-$PEG_{(1000\ or\ 2000)}$-OH, followed by phosphite oxidation with mCPBA, and finally phosphate di-*tert*-butyl ester hydrolysis (Scheme S1, ESI). This noteworthy synthesis approach was preferred to the direct phosphorylation of m-PEG-OH with phosphoryl chloride, which leads to a mixture of mono- and di-phosphate esters as described by JC Boyer *et al*.[32] To synthesize the bis- and tetra-phosphonate PEG derivatives, L3-L10, a convergent plan was developed, based on the amide bond formation between *N*-hydroxysuccinimide activated-acid of m-$PEG_{(1000\ or\ 2000)}$-CO_2H (S12a,b in ESI) and amine functionalized bis or tetra-phosphonate ester key intermediates (S6, S11, S19 and S21, respectively in ESI), followed by transesterification with bromotrimethylsilane and methanolysis of the corresponding silyl phosphonate esters under mild conditions (Schemes S2 and S3, ESI). All the final hydrophilic ligands were obtained with a high degree of purity, according to MALDI-TOF, FTIR and ^{1}H, ^{13}C and ^{31}P NMR spectroscopies (see detailed protocols and characterizations in ESI).

The hydrophobic UCNP were then subjected to direct ligand exchange with a large excess of PEG ligands compared with UCNP@OA (i.e. 10-fold w/w excess). After removing the free ligands by repeated ultracentrifugation (cut-off 30 kDa), transparent aqueous colloidal solutions of as-prepared UCNP@PEG were obtained, regardless the hydrophilic ligand used. FTIR spectroscopy was then performed to assess the surface coating before and after PEG ligand exchange. As depicted in Fig. 1h for $UCNP@PEG_{(2000)}$ derivatives, the peaks at 2923-2854 cm^{-1} and 1546 cm^{-1}, associated with =C-H and C=O stretching vibrations of OA functions respectively, were not detected. By contrast, several bands belonging to the PEG backbone were identified at 1460 cm^{-1} (CH_2 scissoring), 1340 cm^{-1} (CH_2 wagging), 1240/1280 cm^{-1} (CH_2 twisting), 1100-1080 cm^{-1} (C-O/C-C stretching) and 960-940 cm^{-1} (CH_2 rocking/CH_2 twisting). Furthermore, a peak at 1540-1550 cm^{-1} attributed to C=C conjugated stretching vibrations of the aryl groups for UCNP@L6 and UCNP@L10, was also observed. However, the bands of the PEG chain probably overlapped characteristic absorption signals of phosphate and phosphonate functions (i.e., P=O and P-O bands at approximately 1140-960 and 1100-940 cm^{-1}, respectively, Fig. S5, ESI). The same trend was also observed for $UCNP@PEG_{(1000)}$ family (Fig. S4 and S5, ESI). Overall, these data suggest successful OA to PEG exchange on the nanoparticle surface for all the anchoring groups and PEG chain lengths assessed.

Colloidal stability of the hydrophilized UCNP was then evaluated by DLS in different aqueous solutions. In deionized water (see Fig. 2a), $UCNP@PEG_{(1000)}$ showed irregular hydrodynamic diameters, varying from 49.7 nm to 84.0 nm, at early time points, regardless of the hydrophilic ligand used. Conversely, narrow size distribution (from 46.7 nm to 54.8 nm) was reported for most of the $UCNP@PEG_{(2000)}$ (except for UCNP@L6). After one week (Fig. 2b), instability in deionized water was noticeable for the UCNP coated with ligands

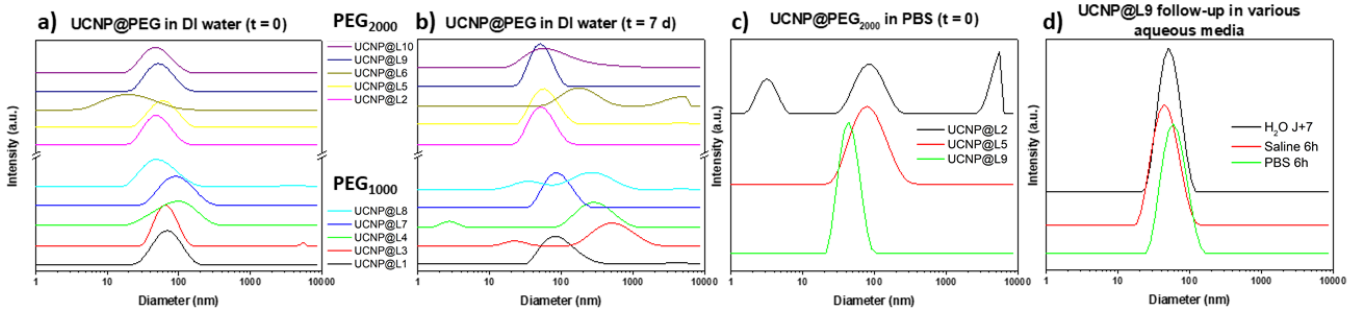

Fig. 2 DLS patterns of particle-size distribution of UCNP@L1-10 in deionized water at (a) t = 0 and (b) t = 7 d (PDI were given in Table S1, ESI), (c) UCNP@L2, @L5, @L9 in PBS at t = 0 and (d) UCNP@L9 after 6 h follow-up in saline and PBS (compared to water at t = 7 d as a reference).

containing shorter polymeric chains and/or aryl spacers (i.e., UCNP@L3, @L4, @L6, @L8 and @L10). On the basis of these results, UCNP@L2, @L5 and @L9 were selected for further analysis in PBS.

DLS patterns showed fast aggregation of UCNP@L2 and UCNP@L5 immediately after dilution in PBS (Fig. 2c). The nanoparticles hydrophilized with $PEG_{(2000)}$ and bearing phosphate or bis-phosphonate surface binding groups were therefore considered unsuitable for biological applications.

In contrast, as shown in Fig. 2d, excellent colloidal stability of the L9-coated UCNP was observed in saline (up to 6 h) and, to a lesser extent, in PBS, with only slightly shifting to larger diameters after 6 h (from 42.8 nm at t = 0 to 60.7 nm at t = 6 h). Further experiments were performed in RPMI and MEM culture media at 37 °C, in anticipation of cell studies. However, the DLS spectra obtained after dilution of UCNP@L9 in such complex solutions were not meaningful and should be interpreted with caution. This is probably due to the presence of fluorophores in the media and persistent foam during the analysis, which could have a negative effect on the light scattering measurements (data not shown). Finally, to evidence the conservation of the optical properties in the NIR range after the OA to PEG exchange, the UCL spectrum of UCNP@L9 in water was recorded (Fig. S7b, ESI).

Together, the superior colloidal stability in aqueous media observed for UCNP coated with hydrophilic ligands bearing multidentate anchoring groups and/or longer PEG chains is consistent with the results reported by Cao *et al.*[35] for similar lanthanide-based nanoparticles. Based on these results, the tetra-phosphonate ligand L9 was selected for further studies.

3.3. Preparation and characterization of functionalized UCNP

To graft prostate-tumour targeting ligands and/or radionuclides onto the surface of UCNP, we opted for the well-known strain-promoted azide-alkyne cycloaddition (SPAAC) reaction between azide and azadibenzocyclooctyne (called ADIBO) because of its fast rate, mild reaction conditions and versatility.[36] As ADIBO is lipophilic and could impair the water solubility of UCNP, azide was first introduced onto the surface of the nanoparticles, requiring synthesis of an azide-ended analogue of L9, called L11. This ligand was obtained from N_3-$PEG_{(2000)}$-OH S26 according to the synthetic pathway developed for L9 with slight modifications (Scheme S4, ESI). Note that direct oxidation of the latter with Jones reagent led to several by-products. Therefore we used an alternative method, involving etherification of S26 with *tert*-butyl bromoacetate followed by ester deprotection with 2N hydrochloric acid.

To investigate the impact of PSMA-inhibitor density on the UCNP surface for PSMA binding specificity, two kinds of UCNP with azide groups or a 10/90 ratio azide/methoxy groups on the surface prepared. The surface ligand density of as-prepared UCNP (called $UCNP@N_{3(10\%)}$ and $UCNP@N_{3(100\%)}$) and UCNP@OA was evaluated by TGA, ICP-AES, and/or radioactive quantitation of the azide groups. On the basis of the work carried out by Tong L *et al.*,[37] and assuming that the as-synthetized UCNP were spherical and that the average molecular weights of ligands when mixture of L9/L11 was used was approximately 2600 g.mol^{-1}, the ligand density (ρ_l, ligand molecules per nm^2) was calculated as follows:

$$\rho_l = \frac{w_l N_{Av}}{M_{w,l}} \cdot \frac{m_{NP}}{(1-w_l)A_{NP}} \qquad (1)$$

where w_l is the weight fraction of the ligand determined by ICP (P/Y ratio), TGA or radioactive quantitation of the azide function, N_{Av} is the Avogadro constant, $M_{w,l}$ is the average molecular weight of the ligands, m_{NP} is the mass of one core/shell UCNP, according to the formula described by Mackenzie L.E. *et al.*,[38] and based on TEM values and Y, Yb, Tm % ICP-MS analysis.

The ligand density calculation for UCNP@OA by TGA gave 4.0 ± 0.1 OA/nm². This result agrees with the data in the literature, which suggest ligand coverage of approximatively 5.9 OA/nm² for smaller sized UCNP (22 nm).[37] For $UCNP@N_3$, TGA gave 1.54 ± 0.11 PEG/nm² and 1.92 ± 0.08 PEG/nm² for $UCNP@N_{3(10\%)}$ and $UCNP@N_{3(100\%)}$, respectively (Table 1). To confirm these results, ICP-AES analysis of hydrophilic UCNP containing tetra-phosphonate ligands were performed. Based on phosphor and yttrium measurements for 2.0 ± 0.1 mg samples, ICP-AES quantification led to ligand density calculation of 0.88 ± 0.03 and 1.69 ± 0.04 ligand/nm² for $UCNP@N_{3(10\%)}$ and $UCNP@N_{3(100\%)}$, respectively. These results agree with the literature, indicating an average of 1.1 to 2.3 ligands/nm², depending on the nature of phosphorus anchoring group, the analysis method and the size of the $NaYF_4$ nanoparticles.[37] For *in vitro/vivo* studies, all calculations were therefore based on an average of 1.3 ligand/nm².

Table 1 Ligand density measurements for $UCNP@N_{3(10\text{ and }100\%)}$

UCNP@PEG (% N_3)	Ligand density (ligand/nm²)		
	TGA	ICP-AES	Radioactive quantification
10%	1.54 ± 0.11	0.88 ± 0.03	1.30 ± 0.05*
100%	1.92 ± 0.08	1.69 ± 0.04	0.92 ± 0.19

*value calculated considering UCNP surface covered with 10% of azide functions

Finally, we investigated an original quantitative, radioactive-based measurement of azide functions involving a radioiodinated ADIBO derivative called [^{125}I]IBA-ADIBO. As illustrated in Scheme S12 (ESI), [^{125}I]IBA-ADIBO was synthetized in two steps by radioiododestannylation of *N*-hydroxysuccinimide 3-tributylstannylbenzoate followed by conjugation with ADIBO-NH_2 (compound S43, ESI). With this procedure, [^{125}I]IBA-ADIBO was obtained in about 3 h with an overall radiochemical yield of 39% and excellent radiochemical purity (>99%). This method was used to determine azide/methoxy ratio on $UCNP@N_{3(10\%)}$ and ligand quantification on $UCNP@N_{3(100\%)}$. For both measurements, increasing known concentrations of ADIBO-CO_2H were left overnight to interact with fixed amounts of $UCNP@N_3$. The resulting solutions was then treated with [^{125}I]IBA-ADIBO (74 kBq) for another 30 min

to assess the remaining free azide functional groups (quantification curves are given in Fig. S9, ESI). For UCNP@$N_{3(10\%)}$, radioactive quantification combined with TGA or ICP-AES ligand density calculations, estimated azide coverage density on UCNP surface at 8.8 ± 0.2% and 13.8 ± 0.4%, respectively. These values were consistent with the 90/10 molar ratio of L9/L11 ligands initially used to hydrophilize UCNP@OA. Surprisingly, when applied to UCNP@$N_{3(100\%)}$, this methodology led to ligand coverage being underestimated compared with TGA and ICP-AES analyses (0.92 ± 0.19 vs 1.92 ± 0.08 and 1.69 ± 0.04 ligand/nm², respectively). This result could be explained by steric hindrance due to ADIBO-CO_2H grafting onto the UCNP@$N_{3(100\%)}$ surface, which might affect the SPAAC radiolabelling.

4. Synthesis and *in vitro* evaluation of PSMA targeted UCNP

Several over-expressed membrane proteins have been studied for the selective targeting of prostate cancer cells. These include integrins[39] and receptors of epidermal growth factor,[40] transferrin,[41] folate[42] and gastrin-releasing peptide.[43] By far the most extensively studied among them is PSMA.[44] This transmembrane glycoprotein receptor is expressed by most PCa, especially the most aggressive ones,[45] with levels 2-3 times higher than in surrounding or distant healthy PSMA-positive tissues (e.g., prostate epithelium, renal proximal tubules, salivary glands).[46] Moreover a broad range of small, glutamic-based organic PSMA inhibitors has been developed such as 2-phosphonomethylpentandioic acid (PMPA) or lysine-glutamic acid urea (KuE) derivatives. The latter are giving rise to a promising new class of radiopharmaceuticals for molecular imaging and targeted radionuclide therapy of PCa.[44]

Based on these results, we first attempted to design KuE-ADIBO conjugates by forming amide bonds between ADIBO-carboxylic acids and the ε-amino function of KuE *tert*-butyl esters, followed by acid-mediated removal of the *tert*-butyl protecting groups. However, all our attempts were unsuccessful (data not shown), probably due to fast rearrangement of the ADIBO moiety into 6*H*-isoindolo[2,1-*a*]indole[47] during the deprotection step. To overcome this limitation, two strategies were designed (Schemes S5-7, ESI): one involving the direct reaction of unprotected KuE with *N*-hydroxysuccinimide-activated ADIBO carboxylic acids, leading to ADIBO-KuE(1-2) with or without a PEG-based linker, and the second involving thiol-maleimide conjugation between unprotected KuE-sulfhydryl and ADIBO-maleimide derivatives, to give ADIBO-KuE3 (Fig. 3a). To confirm that conjugation of the SPAAC functional group does not interfere with PSMA recognition, the ADIBO-KuE conjugates were put through a competitive inhibition assay (IC_{50}) using LNCaP-Luc cells and one of the most powerful radiolabelled PSMA inhibitors [^{125}I]IBA-KuE[29] (Ki = 0.01 ± 0.003 nM), whose radiosynthesis is fully described in ESI. The ADIBO-KuE(1-3) conjugates exhibited higher inhibitory potencies than PMPA, used as a positive control, with IC_{50} values of 32, 135 and 16 nM *vs* 188 nM, respectively. However, it seems that the introduction of a PEG_4 spacer between the ADIBO and KuE residues had a negative impact on PSMA affinity compared with direct amide or thioether ligation. The ADIBO-KuE(1-3) and ADIBO-CO_2H (used as a negative control) were then conjugated onto the surface of UCNP@$N_{3(10\text{ and }100\%)}$, purified by exclusion chromatography and ultracentrifugation, leading to functionalized UCNP with hydrodynamic diameters determined by DLS in the range of 47.5-67.6 nm (PDI 0.100-0.154) (Fig. S10, ESI).

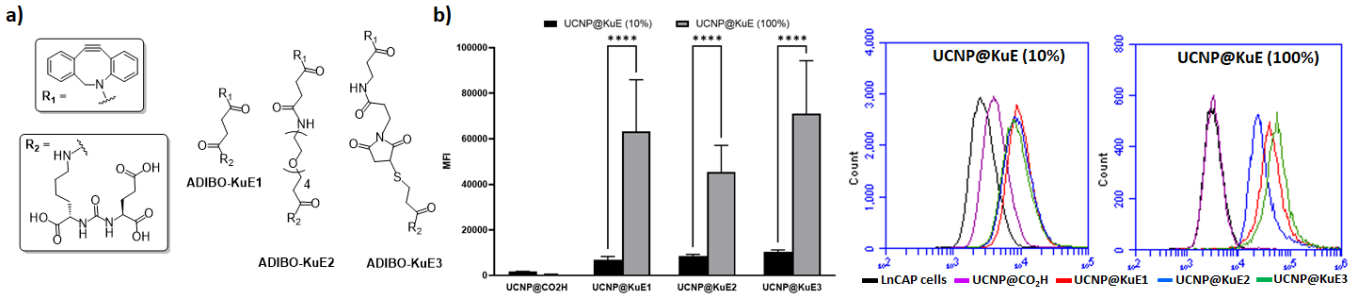

c)

	Surface density of ligands (%)	IC_{50} nM	IC_{50} µg/mL
UCNP@KuE1	10	1.80 ± 0.69	96.0 ± 37.0
	100	0.60 ± 0.09	28.0 ± 4.0
UCNP@KuE2	10	7.95 ± 0.58	425.0 ± 31.0
	100	3.73 ± 0.52	173.0 ± 24.0
UCNP@KuE3	10	1.74 ± 0.84	93.0 ± 45.0
	100	0.37 ± 0.04	17.0 ± 2.0
PMPA		238 ± 43	

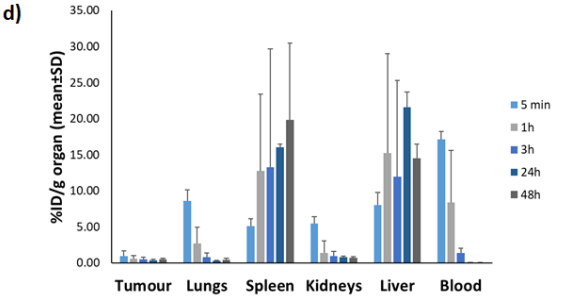

Fig. 3 *In vitro* and *in vivo* evaluations of functionalized UCNP. (**a**) Structures of ADIBO-KuE ligands used for UCNP functionalization. (**b**) Comparison of UCNP@KuE(1-3)$_{(10\text{ and }100\%)}$ binding on LNCaP-Luc by flow cytometry using UCNP@$CO_2H_{(10\text{ and }100\%)}$ as negative control. MFI: mean fluorescence intensity. Typical histograms were shown for each experiment. (**c**) IC_{50} values for UCNP@KuE(1-3)$_{(10\%\text{ and }100\%)}$ in LNCaP-Luc cell line. (**d**) Biodistribution in main organs and tumour at 5 min, 1 h, 3 h, 24 h and 48 h post i.v. injection of [^{125}I]UCNP@$CO_2H_{(10\%)}$ (390 kBq) in LNCaP-Luc xenografted nude mice.

4.1. Cytotoxicity assay

The viability of LNCaP-Luc, PC3-Luc and fibroblasts cells exposed to UCNP@KuE(1-3) or UCNP@CO_2H was investigated for concentrations ranging from 1.2 μg to 1.2 mg/mL and 1.7 μg to 1.7 mg/mL, for 10 and 100% coverage, respectively. Regardless of functionalization or surface density, more than 80% cell survival were observed after 24 h of incubation for the highest concentrations of UCNP (Fig. S11, ESI), indicating that these nanoparticles are not toxic for the three cell lines tested and are highly biocompatible. These results agree with those described in the literature for similar pegylated upconverting nanomaterials[22] highlighting their high level of biocompatibility.

4.2. Competition binding experiment

We then explored the ability of UCNP@KuE to bind with the PSMA in LNCaP-Luc cells. Based on an estimation of UCNP molar mass (calculated with a ligand surface density of 1.3 ligand/nm²), all the actively targeted UCNP showed a lower IC_{50} than the PMPA reference, with values ranging from 1.74 to 7.95 nM and 0.37 to 3.73 nM for 10 and 100% surface densities, respectively compared with 238 ± 43 nM for PMPA (Fig. 3c). As previously observed for ADIBO-KuE(1-3), the nature of the spacer between ADIBO and KuE moieties did not affect the affinity of the UCNP for PSMA. However, introducing a PEG_4 linker had a negative effect on this binding, as shown by the IC_{50} values obtained for UCNP@KuE2$_{(10\text{ and }100\%)}$: ~2.5 to 10-times higher than that of UCNP@KuE1 and UCNP@KuE3.

4.3. Flow cytometry assay

To confirm the results of the competition binding, flow cytometry assays were performed in LNCaP-Luc cells. To this end, and taking advantage of the SPAAC strategy used for surface functionalization, UCNP@$N_{3(10\text{ and }100\%)}$ were covered with a mixture of ADIBO-KuE or -CO_2H ligands doped with commercially available ADIBO-fluorescein (i.e., DBCO-PEG_4-5/6-FAM) in a 99.5/0.5 molar ratio. Using this procedure, fluorescein and PSMA-targeting ligands were independently grafted onto UCNP surface allowing objective assessment of binding. As expected, UCNP@$CO_2H_{(10\text{ and }100\%)}$ did not bind to LNCaP-Luc cells, showing MFI values similar to those of the cells alone (Fig. 3b). For the active targeted UCNP@KuE(1-3)$_{(10\%)}$, we observed significant binding compared with UCNP@$CO_2H_{(10\%)}$. This binding was further enhanced with UCNP@KuE(1-3)$_{(100\%)}$, compared with the 10% functionalized, inducing a dramatic increase of MFI. Finally, for each UCNP@KuE(1-3)$_{(10\text{ and }100\%)}$, MFI corroborated the IC_{50} results, with UCNP@KuE(1,3) binding being higher than UCNP@KuE2. Note that similar experiments were performed to assess the specific binding of PSMA-nanobubbles on both PSMA-positive and -negative cells.[48] We also showed by flow cytometry that the UCNP$_{(10\%)}$ did not bind to PC3-Luc cells (data not shown).

4.4. Cellular uptake and *in vivo* biodistribution

Prior to perform in-depth imaging evaluation in animal models, the impact of UCNP radiolabelling in terms of antigen recognition, *in vivo* stability and passive tumour targeting was explored. The cellular uptake of functionalized UCNP in LNCaP-Luc cells was determined after SPAAC radiolabelling with Iodine-125. This gamma-emitting radionuclide was chosen to radiolabel the UCNP for its ease of detection, commercial availability and physical half-life ($T_{1/2}$ = 59.41 d), which is high enough to perform long-term biodistribution studies. For cellular uptake assay, UCNP@$N_{3(100\%)}$ were radiolabelled with [^{125}I]IBA-ADIBO prior to functionalization with either ADIBO-KuE3, one of the most potent PSMA-targeting ligand identified previously, or ADIBO-CO_2H, used as a control. After purification, the corresponding radioiodinated UCNP were obtained with radiochemical yields ranging from 78 to 83%. LNCaP-Luc cells were then incubated with 18.5 kBq of [^{125}I]UCNP@KuE3$_{(100\%)}$ or [^{125}I]UCNP@$CO_2H_{(100\%)}$ for 1 h at 37 °C. Although radioactive uptake by the cells of non-targeted [^{125}I]UCNP@$CO_2H_{(100\%)}$ (2.2 ± 0.9%) remained very low, values as high as 21.0 ± 7.8% were obtained for PSMA-targeted UCNP@KuE3$_{(100\%)}$. Finally, considering that the Enhance Permeation and Retention (EPR) effect could play an essential role in the delivery of nanostructures in tumours, we made a preliminary biodistribution study of non-targeted [^{125}I]UCNP@$CO_2H_{(10\%)}$ administered by i.v. route in LNCaP-Luc xenografted nude mice. The study was conducted when tumours exhibited a mean volume of around 500 mm^3. As illustrated in Figure 3d, radioactivity was widely detected in the blood (17.1 ± 1.12 %ID/g), spleen (5.12 ± 0.99 %ID/g), lungs (8.63 ± 1.5 %ID/g), kidneys (5.45 ± 0.97 %ID/g) and liver (8.01 ± 1.78 %ID/g) as early as 5 min after i.v. injection of the radiolabelled UCNP. No evidence of *in vivo* radio-deiodination was observed throughout the study, as highlighted by the low thyroid uptake values obtained at all time points (Table S2, ESI). The accumulation of radiolabelled [^{125}I]UCNP@$CO_2H_{(10\%)}$ in the liver and spleen reached its maximum 24 h p.i., which is in agreement with the pharmacokinetics described in the literature for similar UCNP.[22] However, the rapid accumulation of radioactivity in the spleen, which could be attributable to the mononuclear phagocyte system, raises the question of *in vivo* nanoparticle aggregation. Considering tumour accumulation, low levels of radioactivity were also observed (< 1% of ID/g) and were mainly attributed to circulating activity. Since tumour/blood ratio were < 1 throughout the study, our results suggest that passive tumour-targeting of such UCNP through the EPR effect, was negligible in this animal model.

5. Conclusions

In this study, we developed efficient one-pot synthesis of core/shell $NaYF_4$:Yb,Tm@$NaYF_4$ UCNP@OA with uniform size and shape distribution. After ligand exchange, DLS studies led to the selection of a PEGylated tetra-phosphonate, which ensured the colloidal stability of UCNP in relevant aqueous media. For efficient prostate tumour-targeting, the surface of UCNP was covalently modified with PSMA-targeting ligands using the versatile SPAAC cycloaddition strategy. We demonstrated with competition binding assays and CMF analyses that antigen binding was closely related to the surface density of PSMA targeting ligands on the nanoparticles. For the

as-prepared UCNP, no cytotoxic activity was observed after 24 h of incubation in PSMA-positive and -negative prostate cancer cells, or in fibroblasts, for some at concentrations up to 1.7 mg/mL. Furthermore, radiolabelling of UCNP@KuE3$_{(100\%)}$ with iodine-125 through SPAAC cycloaddition did not compromise the binding to the PSMA antigen in LNCaP-Luc cells, as demonstrated by the uptake assays. Finally, a preliminary biodistribution study with non-targeted [^{125}I]UCNP suggests high *in vivo* stability of the radiolabelled nanocomposites. Taken together, our results indicate that these PSMA-targeted UCNP are promising probes for dual fluorescence and radioactive-guided surgery of prostate cancers.

Conflicts of interest

There are no conflicts to declare.

Acknowledgements

This work was partially supported by the Cancéropôle Lyon Auvergne Rhône Alpes (CLARA), the Clermont Auvergne Métropôle, the Puy de Dôme Department and the Auvergne Rhône Alpes Region (Structuring program: Cancer Auvergne Prostate). The authors would like to thank C. Blavignac (Centre d'Imagerie Cellulaire Santé CICS-UCA Partner, Clermont-Ferrand) for her technical support and expertise in TEM analysis, M. Leremboure (Mass Spectroscopy platform, UMR 6296 CNRS/UCA Partner, Clermont-Ferrand) for HRMS analyses and the staff of the *In Vivo* Imaging In Auvergne platform (IVIA, UCA Partner, Clermont-Ferrand) for their contributions to the biodistribution study. The authors would also like to acknowledge F. Léal for IR analyses and L. Frezet for TGA performing.

References

1 Global Burden of Disease Cancer Collaboration, C. Fitzmaurice, T. F. Akinyemiju, F. H. Al Lami, T. Alam, R. Alizadeh-Navaei, C. Allen, U. Alsharif, N. Alvis-Guzman, E. Amini, B. O. Anderson, *et al*. Global, regional, and national cancer incidence, mortality, years of life lost, years lived with disability, and disability-adjusted life-years for 29 cancer groups, 1990 to 2016: A systematic analysis for the global burden of disease study, *JAMA Oncol.*, 2018, **4**(11), 1553–1568.

2 D. A. Woodrum, A. Kawashima, K. R. Gorny and L. A. Mynderse, Prostate cancer: state of the art imaging and focal treatment, *Clin. Radiol.*, 2017, **72**(8), 665-679.

3 O. Yossepowitch, A. Briganti, J. A. Eastham, J. Epstein, M. Graefen, R. Montironi and K. Touifer, Positive surgical margins after radical prostatectomy: a systematic review and contemporary update, *Eur. Urol.*, 2014, **65**(2), 303-313.

4 W. Loon Ong, S. M. Evans, T. Spelman, P. A. Kearns, D. G. Murphy and J. L. Millar, Comparison of oncological and health-related quality of life outcomes between open and robot-assisted radical prostatectomy for localized prostate cancer – findings from the population-based Victorian prostate cancer registry, *BJU Int.*, 2016, **118**(4), 563-569.

5 M. L. Lindenberg, B. Turkbey, E. Mena and P. L. Choyke, Imaging locally advanced, recurrent, and metastatic prostate cancer, a review, *JAMA Oncol.*, 2017, **3**(10), 1415-1422.

6 H. J. Wester and M. Schottelius, PSMA-targeted radiopharmaceuticals for imaging and therapy, *Semin. Nucl. Med.*, 2019, **49**(4), 302-312.

7 S. Sheikhbahaei, A. Afshar-Oromieh, M. Eiber, L. B. Solnes, M. S. Javadi, A. E. Ross, K. J. Pienta, M. E. Allaf, U. Haberkorn, M. G. Pomper, M. A. Gorin and S. P. Rowe, Pearls and pitfalls in clinical interpretation of prostate-specific membrane antigen (PSMA)-targeted PET imaging, *Eur. J. Nucl. Med. Mol. Imaging*, 2017, **44**(12), 2117-2136.

8 S. Ghafoor, I. A. Burger and A. H. Vargas, Multimodality imaging of prostate cancer, *J. Nucl. Med.*, 2019, **60**(10), 1350-1358.

9 C. Qin, J. Zhong, Z. Hu, X. Yang and J. Tian, Recent advances in Cerenkov luminescence and tomography imaging, *IEEE J. Sel. Top. Quantum Electron.*, 2012, **18**(3), 1084-1093.

10 T. Song, X. Liu, Y. Qu, H. Liu, C. Bao, C. Leng, Z. Hu, K. Wang and J. Tian, A novel endoscopic Crenkov luminescence imaging system for intraoperative surgical navigation, *Mol. Imaging*, 2015, **14**, 443-449.

11 F. W. B. van Leewen and H.G. van der Poel, Surgical guidance in prostate cancer: "from molecule to man" translations, *Clin. Cancer Res.*, 2016, **22**(6), 1304-1306.

12 F. W. B. Van Leewen, R. Valdés-Olmos, T. Buckle and S. Vidal-Sicart, Hybrid surgical guidance based on the integration of radionuclear and optical properties, *Br. J. Radiol.*, 2016, **89**(1062), 20150797.

13 Z. Hu, C. C. Chi, M. Liu, H. Guo, Z. Zhang, C. Zeng, J. Ye, J. Wang, J. Tian, W. Yang and W. Xu, Nanoparticle-mediated radiopharmaceutical-excited fluorescence molecular imaging allows precise image-guided tumor-removal surgery, *Nanomedicine*, 2017, **13**(4), 1323-1331.

14 Y. Zhao, T. M. Shaffer, S. Das, C. Pérez-Medina, W. J. M. Mulder and J. Grimm, Near-infrared quantum dot and 89Zr dual-labeled nanoparticles for in vivo Cerenkov imaging, *Bioconjugate Chem.*, 2017, **28**(2), 600-608.

15 Z. Hu, M. Zhao, Y. Qu, X. Zhang, M. Zhang, M. Liu, H. Guo, Z. Zhang, J. Wang, W. Yang and J. Tian, In vivo 3-dimensional radiopharmaceutical-excited fluorescence tomography, *J. Nucl. Med.*, 2017, **58**(1), 169-174.

16 E. L. Rosenthal, J. M. Warram, E. de Boer, J. P. Basilion, M. A. Biel, M. Bogyo, M. Bouvet, B. E. Brigman, Y. L. Colson, S. R. DeMeester, G. C. Gurtner, T. Ishizawa, P. M. Jacobs, S. Keereweer, J. C. Liao, Q. T. Nguyen, J. M. Olson, K. D. Paulsen, D. Rieves, B. D. Sumer, M. F. Tweedle, A. L. Vahrmeijer, J. P. Weichert, B. C. Wilson, M. R. Zenn, K. R. Zinn and G. M. van Dam, Successful translation of fluorescence navigation during oncologic surgery: a consensus report, *J. Nucl. Med.*, 2016, **57**(1), 144-150.

17 Q. Zheng, M. F. Juette, S. Jockusch, M. R. Wasserman, Z. Zhou, R. B. Altman and S. C. Blanchard, Ultra-stable organic fluorophores for single-molecule research, *Chem. Soc. Rev.*, 2014, **43**(4), 1044-1056.

18 R. Hernandez, S. Heskamp, M. Rijpkema, D. L. Bos, D. M. Goldenberg, W. J. McBride, A. Morgenstern, F. Bruchertseifer, W. Cai and O. C. Boerman, Preventing radiobleaching of cyanine fluorophore enhances stability of nuclear/NIRF multimodality imaging agents, *Theranostics*, 2017, **7**(1), 1-8.

19 M. Schottelius, A. Wurzer, K. Wissmiller, R. Beck, M. Koch, D. Gorpas, J. Notni, T. Buckle, M. N. van Oosterom, K. Steiger, V. Ntziachristos, M. Schwaiger, F. W. B. van Leeuwen and H. J. Wester, Synthesis and preclinical characterization of the PSMA-targeted hybrid tracer PSMA-I&F for nuclear and fluorescence imaging of prostate cancer, *J. Nucl. Med.*, 2019, **60**(1), 71-78.

20 A. C. Baranski, M. Schäfer, U. Bauder-Wüst, M. Roscher, J. Schmidt, E. Stenau, T. Simpfendörfer, D. Teber, L. Maier-Hein, B. Hadaschik, U. Haberkorn, M. Eder and K. Kopka, PSMA-11 derived dual-labeled PSMA-inhibitors for preoperative PET imaging and precise fluorescence-guided surgery of prostate cancer, *J. Nucl. Med.*, 2018, **59**(4), 639-645.

21 S. Lütje, M. Rijpkema, D. M. Goldenberg, C. M. van Rij, R. M. Sharkey, W. J. McBride, G. M. Franssen, C. Frielink, W. Helfrich, W. J. G. Oyen and O. C. Boerman, Pretargeted dual-modality immune-SPECT and near-infrared fluorescence imaging for image-guided surgery of prostate cancer, *Cancer Res.*, 2014, **74**(21), 6216-6223.

22 A Gnach, T Lipinski, A Bednarkiewicz, J Rybka and J. A. Capobianco, Upconverting nanoparticles: assessing the toxicity, *Chem. Soc. Rev.*, 2015, **44**(6), 1561-1584.

23 X. Zhu, J. Zhang, J. Liu and Y. Zhang, Recent progress of rare-earth doped upconversion nanoparticles: synthesis, optimization and applications, *Adv. Sci.*, 2019, **6**(22), 1901358.

24 L.Cheng, C. Wang and Z. Liu, Upconversion nanoparticles and their composite nanostructures for biomedical imaging and cancer therapy, *Nanoscale*, 2013, **5**(1), 23-37.

25 G. Chen, H. Qiu, P. N. Prasad and X. Chen, Upconversion nanoparticles: design, nanochemistry, and applications in theranostics, *Chem. Rev.*, 2014, **114**(10), 5161-5214.

26 A. Sedlmeier and H. H. Gorris, Surface modification and characterization of photon-upconverting nanoparticles for bioanalytical applications, *Chem. Soc. Rev.*, 2015, **44**(6), 1526-1560.

27 C. Duan, L. Liang, L. Li, R. Zhang and Z. P. Xu, Recent progress in upconversion luminescence nanomaterials for biomedical applications, *J. Mater. Chem. B*, 2018, **6**(2), 192-209.

28 N. Francolon, D. Boyer, F. Leccia, E. Jouberton, A. Walter, C. Bordeniau, A. Parat, D. Felder-Flesh, S. Begin-Colin, E. Miot-Noirault, J. M. Chezal and R. Mahiou, Preparation of core/shell $NaYF_4$:Yb,Tm@dendrons nanoparticles with enhanced upconversion luminescence for in vivo imaging, *Nanomedicine*, 2016, **12**(7), 2107-2113.

29 Y. Chen, C. A. Foss, Y. Byun, S. Nimmagadda, M. Pullambhatla, J. J. Fox, M. Castanares, S. E. Lupold, J. W. Babich, R. C. Mease and M. G. Pomper, Radiohalogenated prostate-specific membrane Antigen (PSMA)-based ureas as imaging agents for prostate cancer, *J. Med. Chem.*, 2008, **51**, 7933-7943.

30 X. Ge, L. Sun, L. Shi and R. Wei, The modified upconversion nanomaterials (UCNMs) for multimodal imaging and therapies, *Biomed. Spectrosc. Imaging*, 2015, **4**(4), 391-412.

31 J. V. Jokerst, T. Lobovkina, R. N. Zare and S. S. Gambhir, Nanoparticle PEGylation for imaging and therapy, *Nanomedicine*, 2011, **6**(4), 715-728.

32 J. C. Boyer, M. P. Manseau, J. I. Murray and F. C. J. M. van Veggel, Surface modification of upconverting $NaYF_4$ nanoparticles with PEG-phosphate ligands for NIR (800 nm) biolabeling within the biological window, *Langmuir*, 2010, **26**(2), 1157-1164.

33 X. Cui, D. Mathe, N. Kovács, I. Horváth, M. Jauregui-Osoro, R. T. Martin de Rosales, G. E. D. Mullen, W. Wong, Y. Yan, D. Krüger, A. N. Khlobystov, M. Gimenez-Lopez, M. Semjeni, K. Szigeti, D. S. Veres, H. Lu, I. Hernández, W. P. Gillin, A. Protti, K. Kis Petik, M. A. Green, P. J. Blower, Synthesis, characterization and application of core-shell $Co_{0.16}Fe_{2.84}O_4$@$NaYF_4$(Yb, Er) and Fe_3O_4@$NaYF_4$(Yb, Tm) nanoparticle as trimodal (MRI, PET/SPECT, and optical) imaging agents, *Bioconjug. Chem.*, 2016, **27**(2), 319-328.

34 G. Zhao, L. Tong, P. Cao, M. Nitz and M. A. Winnik, Functional PEG-PAMAM-tetraphosphonate capped $NaLnF_4$ nanoparticles and their colloidal stability in phosphate buffer, *Langmuir*, 2014, **30**(23), 6980-6989.

35 P. Cao, L. Tong, Y. Hou, G. Zhao, G. Guerin, M. A. Winnik and M. Nitz, Improving lanthanide nanocrystal colloidal stability in competitive aqueous buffer solutions using multivalent PEG-phosphonate ligands, *Langmuir*, 2012, **28**(35), 12861-12870.

36 C. P. Ramil and Q. Lin, Bioorthogonal chemistry: strategies and recent developments, *Chem. Commun.*, 2013, **49**(94), 11007-11022.

37 L. Tong, E. Lu, J. Pichaandi, P. Cao, M. Nitz and M. A. Winnik, Quantification of surface ligands on $NaYF_4$ nanoparticles by three independent analytical techniques, *Chem. Mater.*, 2015, **27**(13), 4899-4910.

38 L. E. Mackenzie, J. A. Goode, A. Vakurov, P. P. Nampi, S. Saha, G. Jose and P. A. Millner, The theoretical molecular weight of $NaYF_4$: RE upconversion nanoparticles, *Sci. Rep.*, 2018, **8**(1), 1106.

39 E. Lucente, H. Liu, Y. Liu, X. Hu, E. Lacivita, M. Leopoldo and Z. Cheng, Novel ^{64}Cu labelled RGD_2-BBN heterodimers for PET imaging prostate cancer, *Bioconjug. Chem.*, 2018, **29**(5), 1595-1604.

40 T. Fozing, C. Scheuer and S. Samnick, Synthesis and initial tumor affinity testing of iodine-123 labelled EGFR-affine agents as potential imaging probes for hormone-refractory prostate cancer, *Eur. J. Med. Chem.*, 2010, **45**(9), 3780-3786.

41 C. S. Kang, N. Wu, Y. Chen, X. Sun, N. Bandara, D. Liu, M. R. Lewis, B. E. Rogers and H. S. Chong, Transferrin conjugates of triazacyclononane-based bifunctional NE3TA chelates for PET imaging: synthesis, Cu-64 radiolabeling, and in vitro and in vivo evaluation, *J. Inorg. Chem.*, 2016, **154**, 60-66.

42 O. Changizi, S. Khoei, A. Mahdavian, S. Shirvalilou, S. R. Mahdavi and J. K. Rad, Enhanced radiosensitivity of LNCaP prostate cancer cell line by gold-photoactive nanoparticles modified with folic acid, *Photodiagnosis Photodyn. Ther.*, 2020, **29**, 101602.

43 A. Pagoto, F. Garello, G. M. Marini, M. Tripepi, F. Arena, P. Bardini, R. Stefania, S. Lanzardo, G. Valbusa, F. Porpiglia, M. Manfredi, S. Aime and E. Terreno, Novel gastrin-releasing peptide receptor targeted near-infrared fluorescence dye for image-guided surgery of prostate cancer, *Mol. Imaging Biol.*, 2020, **22**(1), 85-93.

44 T. Wüstemann, U. Haberkorn, J. Babich and W. Mier, Targeting prostate cancer: Prostate-specific membrane antigen based diagnosis and therapy, *Med. Res. Rev.*, 2019, **39**(1), 40-69.

45 D. G. Bostwick, A. Pacelli, M. Blute, P. Roche and G. P. Murphy, Prostate specific membrane antigen expression in prostatic intraepithelial neoplasia and adenocarcinoma: a study of 184 cases, *Cancer*, 1998, **82**(11), 2256-2261.

46 R. L. Sokoloff, K. C. Norton, C. L. Gasior, K. M. Marker and L.S. Grauer, A dual-monoclonal sandwich assay for prostate-specific membrane antigen: levels in tissues, seminal fluid and urine, *Prostate*, 2000, **43**(2),150-157.

47 M. F. Debets, S. S. van Berkel, S. Schoffelen, F. P. J. T. Rutjes, J. C. M. van Hest and F. L. van Delft, Aza-dibenzocyclooctynes for fast and efficient enzyme PEGylation via copper-free (3+2) cycloaddition, *Chem. Commun.*, 2010, **46**(1), 97-99.

48 Y. Wang, M. Lan, D. Shen, K. Fang, L. Zhu, Y. Liu, L. Hao and P. Li, Targeted nanobubbles carrying indocyanine green for ultrasound, photoacoustic and fluorescence imaging of prostate cancer, Int. J. *Nanomedicine*, 2020, **15**, 4289-4309.

Author Contributions

Axel Cordonnier: methodology, investigation, writing
Damien Boyer: conceptualization, writing, reviewing and editing
Sophie Besse: investigation
Rodolphe Valleix: investigation
Rachid Mahiou: investigation
Mercedes Quintana: investigation
Arnaud Briat: investigation
Mhammed Benbakkar: investigation
Frédérique Penault-Llorca: reviewing
Aurélie Maisonial-Besset: investigation
Benoit Maunit: investigation
Sébastien Tarrit: investigation
Magali Vivier: investigation
Tiffany Witkowski: investigation
Leslie Mazuel: methodology, investigation
Françoise Degoul: methodology, investigation, reviewing
Elisabeth Miot-Noirault: methodology, reviewing
Jean-Michel Chezal: conceptualization, methodology, writing, reviewing and editing, supervision